Electronic Supplementary Information

Exploiting enzymes to optimize pH-universal electrocatalytic ORR performance of biomass-based nanoporous carbons

Huifen Wang, Xiao Kong, Wendu Zhang, Peiyao Bai, Chuangchuang Yang, Weiqi Liu, Shilin Wei, Lang Xu*

MOE Key Laboratory of Coal Processing and Efficient Utilization, School of Chemical Engineering and Technology, China University of Mining and Technology, 1 Daxue Road, Xuzhou, Jiangsu, 221116, China

*Corresponding author. *E-mail address: lang.xu@cumt.edu.cn* (L. Xu)

Physicochemical characterization

Methylene blue (MB) absorption experiments were performed using the following procedure: 1.0 g of CTL, 1.0 g of CE-CTL and 1.0 g of HE-CTL were separately immersed in 50 mL of 0.5 mg mL^{-1} MB aqueous solution and stirred continuously for 24 hours. After that, the resulting supernatants were diluted 20-fold and their absorbances were measured at 664 nm using a UV-vis spectrometry (Shimadzu UV-1780). The absorbance data obtained were used to calculate the uptake levels of MB for samples as follows:

$$Q = (C_0 – C_1) \bullet V / m$$

$$C_1 = A_1 \bullet C_0 / A_0$$

where Q: uptake level, mg g^{-1}; C_0: mass concentration of starting MB solution, mg mL^{-1}; C_1: mass concentration of sample, mg mL^{-1}; V: volume of MB solution, mL; m: sample mass, g; A_0: absorbance of standard MB; A_1: absorbance of sample.

Morphologies of samples were presented by transmission electron microscopy (TEM), high-resolution TEM (HRTEM) and selected area electron diffraction (SAED) using an FEI Tecnai G2 F20 field-emission microscope. Raman spectra were recorded on a Bruker Senterra confocal Raman spectrometer with a 532 nm laser excitation wavelength. Dinitrogen adsorption-desorption isothermal measurements were undertaken on a Quantachrome Autosorb-iQ instrument at 77 K. The quenched-solid density functional theory (DFT) model incorporated in the AsiQwin Software (Version 5.2) was adopted to investigate the DFT surface areas and nanopore width distributions. Chemical states of samples were probed by X-ray photoelectron spectroscopy (XPS) using a Thermo Fisher ESCALAB 250Xi spectroscope with an excitation source of Al-Kα radiation (1486.6 eV).

Electrochemical measurements

Electrochemical experiments in this study were carried out using an Ivium electrochemical workstation (IviumStat.h, Ivium Technologies) combined with an electrode rotator (AFMSRCE, Pine Research) at 25 °C in a standard three-electrode cell which was composed of a rotating disk electrode (RDE) or rotating ring-disk electrode (RRDE) as a working electrode, a reference electrode (Ag/AgCl, 3.5 M KCl, connected to the main cell via a Luggin capillary) and a counter electrode (platinum coil).

To make a catalyst ink for the working electrode, biomass-based sample (3.0 mg) or commercial 20% Pt/C (1.0 mg) was blended with isopropanol (70 μL), 5 wt% Nafion perfluorinated resin solution (10 μL) and ultrapure water (170 μL) under ultrasonication. The resulting ink was transferred to the polished RDE (disk: glassy carbon) or RRDE (disk: glassy carbon, ring: Pt) by pipette, and the loadings of the biomass-based sample and Pt/C were controlled to be 0.5 and 0.2 mg cm^{-2}, respectively.

Electrochemical measurements were performed in 0.1 M KOH (pH = 13), 0.1 M potassium phosphate buffer solution (PBS, pH = 7.0) or 0.5 M H_2SO_4 (pH = 0) saturated with pure dioxygen or dinitrogen gas. All the measured potentials were converted to the reversible hydrogen electrode (RHE):

$$E_{vs.RHE} = E_{vs.Ag/AgCl} + E^{\theta}_{Ag/AgCl} + 0.0591 \times pH$$

Linear sweep voltammograms were recorded at 1600 rpm on the RDE, while cyclic voltammetric experiments were undertaken with no rotation. Voltammetric measurements on the RRDE were conducted at 1600 rpm. Chronoamperometric investigations used for the stability and methanol-tolerance tests were carried out at a rotation rate of 400 rpm with the fixed potentials of 0.67 V vs. RHE (alkaline), 0.57 V vs. RHE (neutral) and 0.50 V vs. RHE (acidic).

The Koutecky–Levich (K–L) equation was used to calculate the electron-transfer number (n):

$$\frac{1}{j} = \frac{1}{j_L} + \frac{1}{j_K} = \frac{1}{B\omega^{1/2}} + \frac{1}{j_K}$$

where j is the measured current density (mA cm^{-2}), j_L is the limiting current density (mA cm^{-2}), j_K is the kinetic current density (mA cm^{-2}), ω is the rotating rate of RDE (rpm), and B is the Levich constant, which is given by:

$$B = 0.2nFC_0(D_0)^{2/3}v^{-1/6}$$

where F is the Faraday constant (96485 C mol^{-1}), C_0 is the bulk concentration of O_2 ($1.2 \cdot 10^{-3}$ mol L^{-1}), D_0 is the O_2 diffusion coefficient ($1.9 \cdot 10^{-5}$ cm^2 s^{-1}), v is the kinetic viscosity (0.01 cm^2 s^{-1}).

In the RRDE measurements, the n values and the percentages of peroxide (*peroxide*%) produced were calculated according to the following equations:

$$n = 4\frac{I_d}{I_d + I_r/N}$$

$$peroxide\% = 200\frac{I_r/N}{I_d + I_r/N}$$

where I_d is the disk current density, I_r is the ring current density and N is the current collection efficiency of the Pt ring (0.37).

Tafel slopes were calculated according to the Tafel equation:

$$E = a + b\log j_K$$

where E is the applied potential, a is a constant, b is the Tafel slope and j_k is the kinetic current density.

Table S1. Methylene blue uptake capacities of CTL, CE-CTL and HE-CTL.

Material	CTL	CE-CTL	HE-CTL
Uptake Capacity (mg g^{-1})	9.82	19.48	16.87

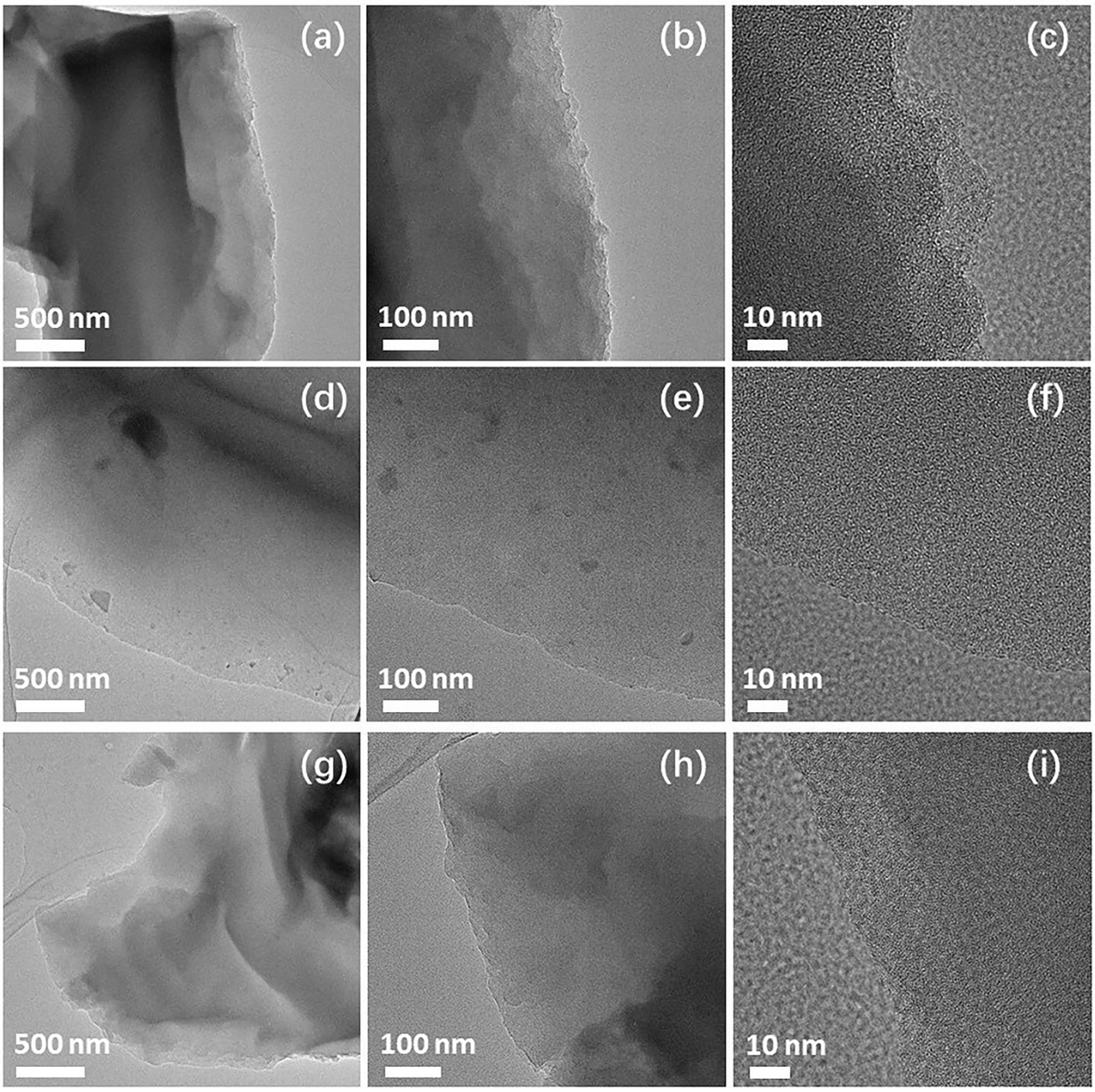

Fig. S1. TEM images of (a-c) PC, (d-f) CE-PC and (g-i) HE-PC.

Table S2. SSAs and volumes of nanopores in PC, CE-PC and HE-PC according to the QSDFT model. [a]

Material	S_{QSDFT} ($m^2\ g^{-1}$)	V_{QSDFT} ($cm^3\ g^{-1}$)	S_{micro} ($m^2\ g^{-1}$)	V_{micro} ($cm^3\ g^{-1}$)	S_{meso} ($m^2\ g^{-1}$)	V_{meso} ($cm^3\ g^{-1}$)
PC	38.21	$3.67*10^{-2}$	26.06	$9.67*10^{-3}$	12.15	$2.70*10^{-2}$
CE-PC	17.43	$2.84*10^{-2}$	0.39	$3.85*10^{-4}$	17.04	$2.80*10^{-2}$
HE-PC	18.98	$3.10*10^{-2}$	0.34	$3.34*10^{-4}$	18.64	$3.07*10^{-2}$

[a] S_{QSDFT}: QSDFT specific surface area; V_{QSDFT}: QSDFT total nanopore volume; S_{micro}: specific surface area of micropores; V_{micro}: pore volume of micropores; S_{meso}: specific surface area of mesopores; V_{meso}: pore volume of mesopores.

Table S3. SSAs and volumes of segmented nanopores in NDPC-900, CE-NDPC-900 and HE-NDPC-900 according to the QSDFT model. [a]

Material	S_{QSDFT} ($m^2\ g^{-1}$)	V_{QSDFT} ($cm^3\ g^{-1}$)	$S_{<0.7nm}$ ($m^2\ g^{-1}$)	$V_{<0.7nm}$ ($cm^3\ g^{-1}$)	$S_{eff\ micro}$ ($m^2\ g^{-1}$)	$V_{eff\ micro}$ ($cm^3\ g^{-1}$)	S_{meso} ($m^2\ g^{-1}$)	V_{meso} ($cm^3\ g^{-1}$)
NDPC-900	1208.10	0.72	350.17	0.09	447.88	0.22	410.05	0.41
CE-NDPC-900	1317.07	0.81	384.92	0.10	492.37	0.25	439.78	0.46
HE-NDPC-900	1507.04	0.89	459.22	0.12	556.48	0.28	491.34	0.49

[a] S_{QSDFT}: QSDFT specific surface area; V_{QSDFT}: QSDFT total nanopore volume; $S_{<0.7nm}$: specific surface area of micropores with width <0.7 nm; $V_{<0.7nm}$: pore volume of micropores with width <0.7 nm; $S_{eff\ micro}$: specific surface area of micropores with width from 0.7 to 2 nm; $V_{eff\ micro}$: pore volume of micropores with width from 0.7 to 2 nm; S_{meso}: specific surface area of mesopores; V_{meso}: pore volume of mesopores.

Table S4. Brunauer-Emmett-Teller (BET) specific surface areas and total pore volumes of NDPC-900, CE-NDPC-900 and HE-NDPC-900. [a]

Material	S_{BET} ($m^2\ g^{-1}$)	V_{BET} ($cm^3\ g^{-1}$)
NDPC-900	1301.29	0.91
CE-NDPC-900	1423.44	1.11
HE-NDPC-900	1616.77	1.12

[a] S_{BET}: BET specific surface area; V_{BET}: total pore volume.

Table S5. Contents of carbon, nitrogen and oxygen of NDPC-900, CE-NDPC-900 and HE-NDPC-900 and their relative contents of pyridinic-N, pyrrolic-N, graphitic-N and oxidized-N.

Material	Carbon (at) %	Nitrogen (at) %	Oxygen (at) %	Pyridinic-N (%)	Pyrrolic-N (%)	Graphitic-N (%)	Oxidized-N (%)
NDPC-900	90.80	2.00	7.21	20.12	28.71	26.79	24.38
CE-NDPC-900	89.90	3.54	6.56	30.52	31.46	21.39	16.63
HE-NDPC-900	88.91	4.13	6.96	32.84	27.19	28.78	11.19

Table S6. Absolute amounts of pyridinic-N, pyrrolic-N, graphitic-N and oxidized-N in NDPC-900, CE-NDPC-900 and HE-NDPC-900.

Material	Pyridinic-N (at%)	Pyrrolic-N (at%)	Graphitic-N (at%)	Oxidized-N (at%)
NDPC-900	0.40	0.57	0.54	0.49
CE-NDPC-900	1.08	1.11	0.76	0.59
HE-NDPC-900	1.36	1.12	1.19	0.46

Table S7. Key parameters of ORR for NDPC-900, CE-NDPC-900, HE-NDPC-900 and 20% Pt/C. [a]

Material	Alkaline			Neutral			Acidic		
	E_{onset} V	$E_{1/2}$ V	J_L mA cm^{-2}	E_{onset} V	$E_{1/2}$ V	J_L mA cm^{-2}	E_{onset} V	$E_{1/2}$ V	J_L mA cm^{-2}
NDPC-900	0.98	0.81	4.87	0.88	0.67	4.78	0.82	0.60	4.48
CE-NDPC-900	0.99	0.84	5.11	0.89	0.70	5.28	0.83	0.71	5.07
HE-NDPC-900	1.01	0.85	5.48	0.91	0.73	5.55	0.88	0.73	5.62
20% Pt/C	1.00	0.80	5.30	0.94	0.65	5.38	0.88	0.62	5.30

[a] E_{onset}: onset potential; $E_{1/2}$: half-wave potential; J_L: limiting current density. All the potentials were converted into reversible hydrogen electrodes (RHE).

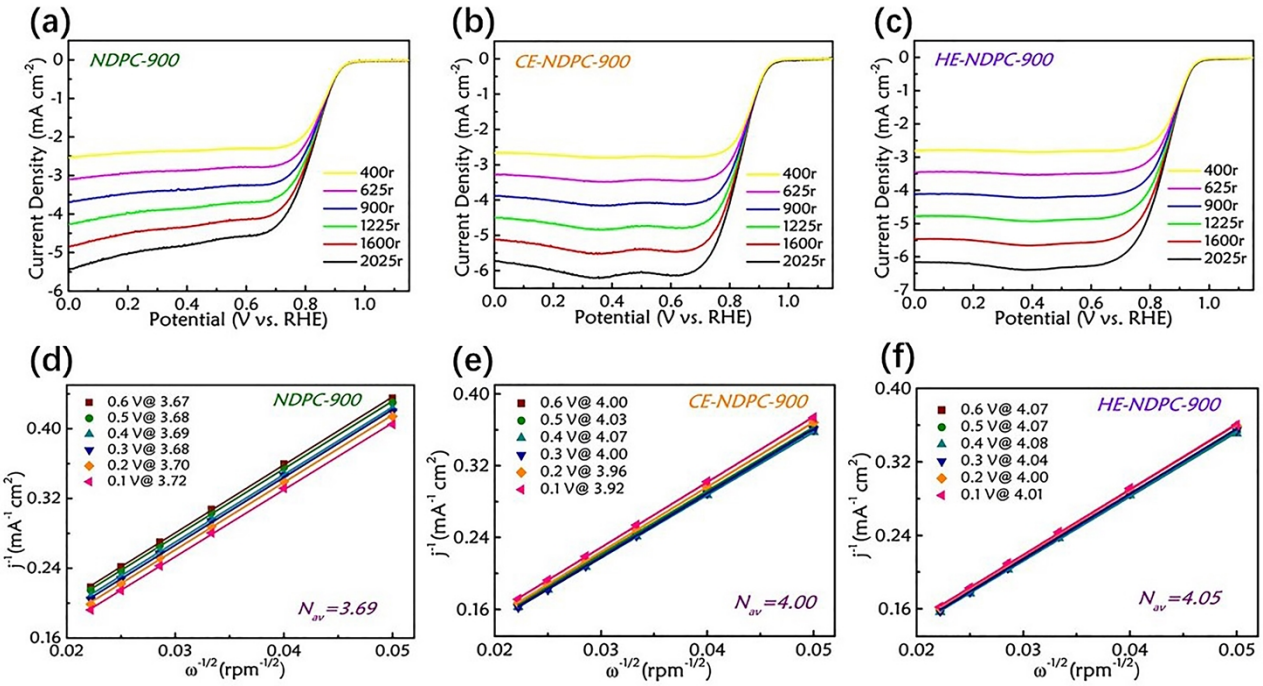

Fig. S2. LSVs of (a) NDPC-900, (b) CE-NDPC-900 and (c) HE-NDPC-900 at different rotation rates and K-L plots of (d) NDPC-900, (e) CE-NDPC-900 and (f) HE-NDPC-900 in O_2-saturated 0.1 M KOH.

Table S8. Average *n* values and peroxide yields of NDPC-900, CE-NDPC-900, HE-NDPC-900 and 20% Pt/C in 0.1 M KOH (0-0.9 V vs. RHE), 0.1 M PBS (0.1-0.8 V vs. RHE) and 0.5 M H_2SO_4 (0.1-0.8 V vs. RHE).

Material	Alkaline		Neutral		Acidic	
	n	*peroxide%*	*n*	*peroxide%*	*n*	*peroxide%*
NDPC-900	3.91	4.46	3.87	6.69	3.86	7.02
CE-NDPC-900	3.93	3.43	3.91	4.38	3.88	5.96
HE-NDPC-900	3.95	2.65	3.93	3.52	3.94	2.77
20% Pt/C	3.96	2.18	3.91	4.72	3.91	4.43

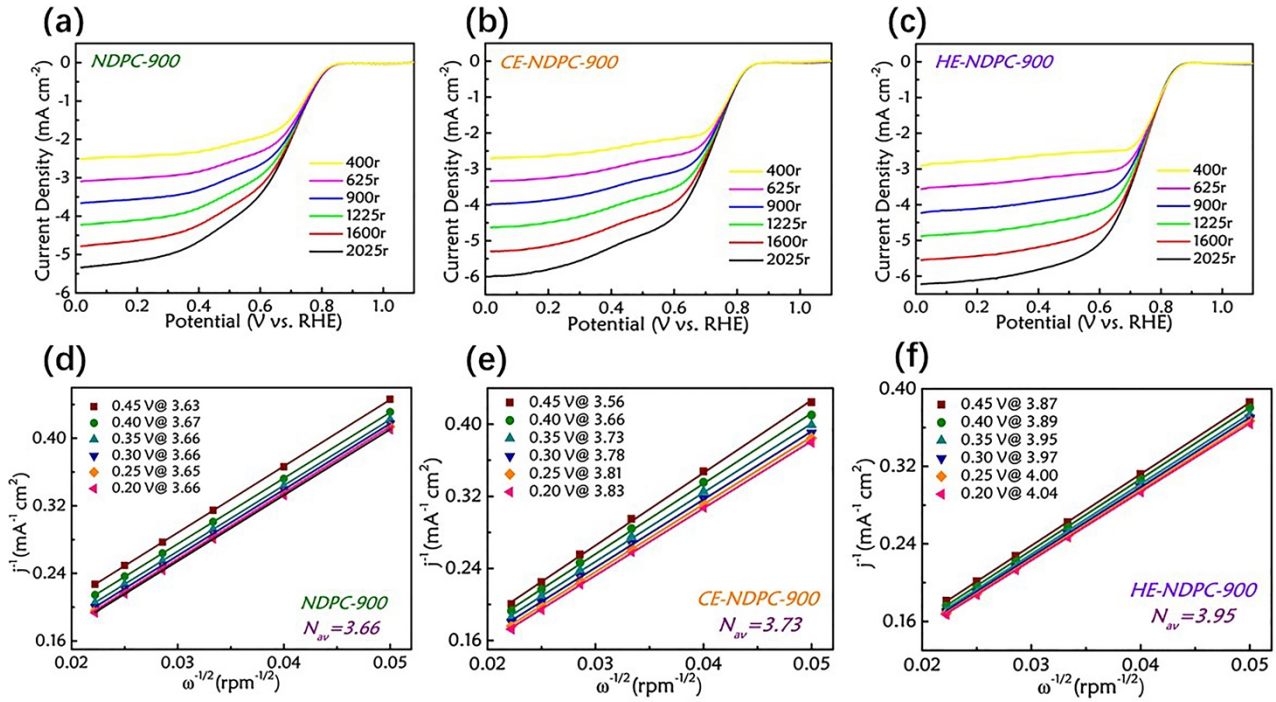

Fig. S3. LSVs of (a) NDPC-900, (b) CE-NDPC-900 and (c) HE-NDPC-900 at different rotation rates and K-L plots of (d) NDPC-900, (e) CE-NDPC-900 and (f) HE-NDPC-900 in O_2-saturated 0.1 M PBS.

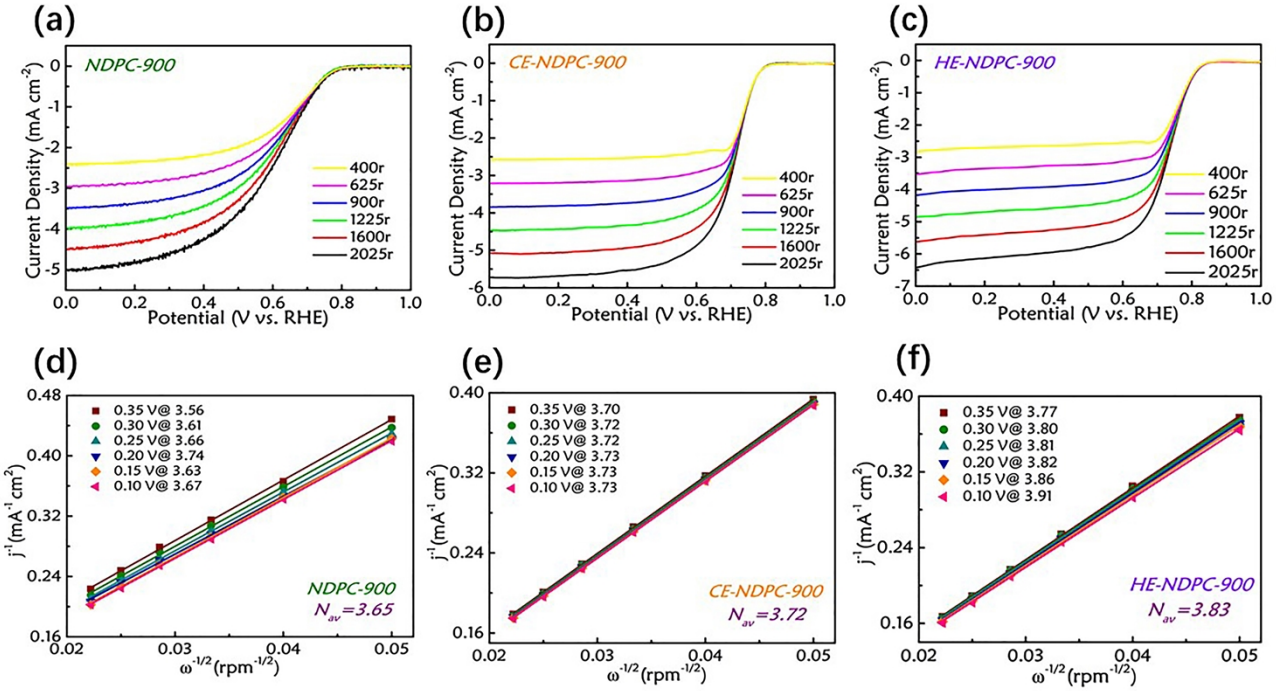

Fig. S4. LSVs of (a) NDPC-900, (b) CE-NDPC-900 and (c) HE-NDPC-900 at different rotation rates and K-L plots of (d) NDPC-900, (e) CE-NDPC-900 and (f) HE-NDPC-900 in O_2-saturated 0.5 M H_2SO_4.

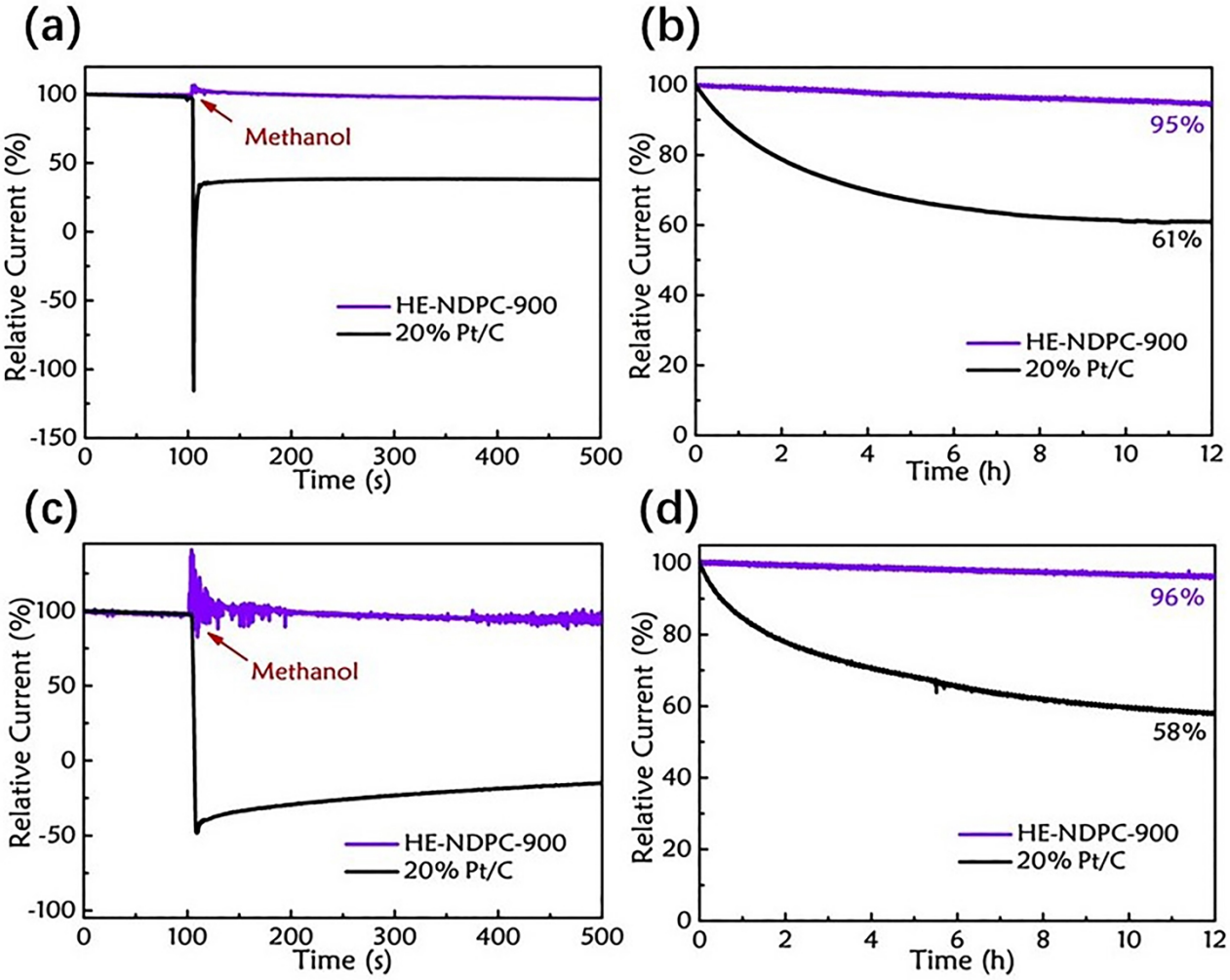

Fig. S5. Chronoamperometric responses for methanol tolerance tests on HE-NDPC-900 and 20% Pt/C in (a) 0.1 M PBS and (c) 0.5 M H_2SO_4; durability measurements of HE-NDPC-900 and 20% Pt/C in (b) 0.1 M PBS and (d) 0.5 M H_2SO_4.

Table S9. Comparisons of ORR kinetic parameters of HE-NDPC-900 with other recently reported carbon-based electrocatalysts. [a]

Electrocatalyst	0.1 M KOH			0.1 M PBS			0.5 M H_2SO_4		
	E_{onset}	$E_{1/2}$	J_L	E_{onset}	$E_{1/2}$	J_L	E_{onset}	$E_{1/2}$	J_L
HE-NDPC-900	1.01	0.85	5.48	0.91	0.73	5.55	0.88	0.73	5.62
Co/N-C [S1]	0.96	0.83	5.45	—	—	—	—	—	—
CNTs-NC-CCC [S2]	0.96	0.83	5.55	—	—	—	—	—	—
Co–N/S–C-3.5 [S3]	0.87	0.80	4.00	—	—	—	0.85	0.75	3.70
D-PC-1(900) [S4]	1.01	0.83	5.43	—	—	—	0.82	0.60	4.60
Fe@BC-800 [S5]	1.01	0.85	5.30	0.86	0.68	4.20	0.86	0.70	4.70
Fe-N-CA-NH_3 [S6]	0.98	0.85	5.10	0.86	0.65	5.00	0.92	0.65	4.50
CPNC-5-850 [S7]	0.97	0.84	4.96	0.87	0.65	4.90	0.80	0.64	4.60
NOPC [S8]	1.00	0.87	5.38	0.91	0.75	5.20	0.84	0.65	5.27
PS-900 [S9]	1.00	0.85	5.84	0.90	0.73	5.52	0.82	0.70	5.10

[a] E_{onset}: onset potential (V); $E_{1/2}$: half-wave potential (V); J_L: limiting current density (mA cm^{-2}). All the potentials are converted into reversible hydrogen electrodes (RHE).

References

[S1] J. Liu, M. Zhang, L. Zhai, Y. Wang, D. Han, P. Chen, N. Qin, L. Mi, L. Yang, Co-N heteroatomic interface engineering in peanut Shell-Derived porous carbon for enhanced oxygen reduction reaction, J. Colloid Interface Sci. 622 (2022) 971-977.

[S2] X. Zheng, Y. Qian, H. Gong, W. Shi, J. Yan, W. Wang, X. Guo, J. Zhang, X. Cao, R. Yang, Bridge-linking interfacial engineering of triple carbons for highly efficient and binder-free electrodes toward flexible Zn-air batteries, Appl. Catal. B: Environ. 319 (2022) 121937.

[S3] Z. Liu, D. Wang, X. Kou, X. Dong, X. Chi, H. Ma, G. Wang, High-performance oxygen reduction electrocatalysts derived from bimetal-organic framework and sulfur-doped precursors for use in microbial fuel cells, J. Power Sources 521 (2022) 230944.

[S4] Y. Hao, X. Zhang, Q. Yang, K. Chen, J. Guo, D. Zhou, L. Feng, Z. Slanina, Highly porous defective carbons derived from seaweed biomass as efficient electrocatalysts for oxygen reduction in both alkaline and acidic media, Carbon 137 (2018) 93-103.

[S5] X. Ma, Z. Lei, W. Feng, Y. Ye, C. Feng, Living Fe mineral@bacteria encrustation-derived and self-templated preparation of a mesoporous Fe-N-C electrocatalyst with high activity for oxygen reduction, Carbon 123 (2017) 481-491.

[S6] Z. Chen, D. Zhao, C. Chen, Y. Xu, C. Sun, K. Zhao, M.A. Khan, D. Ye, H. Zhao, J. Fang, X.A. Sun, J. Zhang, Reconstruction of pH-universal atomic Fe-N-C catalysts towards oxygen reduction reaction, J. Colloid Interface Sci. 582 (2021) 1033-1040.

[S7] J. Qi, B. Jin, W. Liu, W. Zhang, L. Xu, Converting coals into carbon-based pH-universal oxygen reduction catalysts for fuel cells, Fuel 285 (2021) 119163.

[S8] J. Zhou, Y. He, Y.N. Wang, X.Y. Li, C.L. Xu, Metal-free N and O Co-doped carbon directly derived from bicrystal Zn-based zeolite-like metal-organic frameworks as durable high-performance pH-universal oxygen reduction reaction catalyst, Nanotechnology 32 (2021) 405401.

[S9] L. Yu, C. Yang, W. Zhang, W. Liu, H. Wang, J. Qi, L. Xu, Solvent-free synthesis of N-doped nanoporous carbon materials as durable high-performance pH-universal ORR catalysts, J. Colloid Interface Sci. 575 (2020) 406-415.